THE ASTROPHYSICAL JOURNAL, 377:L57–L60, 1991 August 10

FIRST RESULTS FROM THE GODDARD HIGH-RESOLUTION SPECTROGRAPH: ELEMENTAL ABUNDANCES IN THE DIFFUSE CLOUDS TOWARD ξ PERSEI

JASON A. CARDELLI,[1] BLAIR D. SAVAGE,[1] FREDERICK C. BRUHWEILER,[2] ANDREW M. SMITH,[3]
DENNIS C. EBBETS,[4] KENNETH R. SEMBACH,[1] AND ULYSSES J. SOFIA[1]

Received 1991 March 29; accepted 1991 May 9

ABSTRACT

We present an analysis of high-resolution (3.5 km s^{-1}) observations of ultraviolet interstellar absorption lines of dominant ion stages arising in the diffuse clouds ($5 \le v_{\odot} \le 20$ km s^{-1}) toward ξ Per (HD 24912; O7 IIInf) obtained with the Goddard High-Resolution Spectrograph (GHRS). We report a detection of the weak intersystem line of C II] λ2325 ($W_{\lambda} = 1.42 \pm 0.41$ mÅ). For C, O, and Mg we are able to derive column densities from both weak lines and the damping wings of strongly saturated lines. For Mg, the derived column densities differ by a factor 3. The UV absorption-line measurements have become so accurate that the interpretations are now limited by inaccuracies in atomic *f*-values and our knowledge of solar abundances. Comparison of apparent column densities profiles, $N_a(v)$, between lightly depleted (e.g., O I, Zn II) and heavily depleted (e.g., Cr II, Fe II) species indicates a transition from substantial depletions at $v_{\odot} \approx 7.5$ km s^{-1} to a decrease in depletion of a factor 2 or more for $7.5 < v_{\odot} \le 20$ km s^{-1}. This processing may be related to the proximity of the cloud(s) to the H II region surrounding ξ Per.

Subject headings: interstellar: abundances — interstellar: matter — ultraviolet: spectra —
stars: individual (ξ Persei)

1. INTRODUCTION

The sight line toward the O7.5 IIInf star ξ Per [HD 24912; $V = 4.03$, $E(B-V) = 0.32$] presents an interesting opportunity to study the UV absorption-line characteristics of a diffuse cloud(s) environment with a modest molecular hydrogen fraction ($N(H_2)/[N(\text{H I}) + 2N(H_2)] \approx 0.17$; Bohlin, Savage, & Drake 1978). High-dispersion optical data of K I (Hobbs 1974), Ca II (Marshall & Hobbs 1972), and Ti II (Stokes 1978) indicate the presence of at least three components of varying strength distributed over heliocentric velocities of $5 \le v_{\odot} \le 20$ km s^{-1} (see Gomez-Gonzalez & Lequeux 1975). Such structure in a single sight line is of particular interest in that it can provide important diagnostics for gas/dust corresponding to a range of physical conditions.

2. GHRS ECHELLE OBSERVATIONS AND REDUCTIONS

The ξ Per data discussed here were obtained using both GHRS high-dispersion echelle modes (Ech-A and B) in 1990 October and in 1991 January (for specific instrument details see Duncan & Ebbets 1989 and Cardelli, Ebbets, & Savage 1990a) with the star placed in the 0″.25 by 0″.25 small science aperture (SSA) which, projected onto the 500 channel Digicon science diode array, is approximately the width of a single diode. The data were also obtained with a substep sampling strategy corresponding to two samples per science diode width (3.5 km s^{-1} resolution) and a four position comb addition for the purpose of reducing diode-to-diode variations. For all but the October Ech-B observations, the observing strategy included the procedure FP-SPLIT = 4 (see Duncan & Ebbets 1989) which is intended to reduce photocathode fixed pattern noise/granularity. All exposure times ranged between 3 and 6 minutes. Due to target centering problems in the SSA, all the October data and the January Ech-A data resulted in S/N ≈ 15–20 for individual spectra. For the January Ech-B data, the centering was quite good with a resulting S/N ≈ 80. Finally, all observations were made with the on-board Doppler compensator enabled, which compensates for the orbital motion of the spacecraft.

The raw data processing consisted of converting the raw counts from the 500 science diodes to count rates, adjusting for pulse-counting dead-time losses, particle radiation, dark count events, and pixel-to-pixel sensitivity variations. The individual spectrum sampling substeps were merged to form a single spectrum which in this case (two samples per diode) amounts to spectra of 1000 data points in length. Wavelengths, which were assigned from standard calibration tables, are vacuum over the entire UV range observed and correspond to the heliocentric rest frame. The final reduction procedures included (1) alignment and merging of the individual FP-SPLIT subexposures, (2) correction for the effects of echelle grating scattered light background, and (3) assessment of and corrections to the assigned wavelengths. For the individual FP-SPLIT subexposures, effects such as changes in the Digicon deflection caused by Earth's magnetic field, thermal drifts, and slight positioning errors of the carousel, resulted in slight wavelength shifts of spectral features between the individual subexposures. To preserve the full instrumental resolution capability, we employed a procedure which used the positions of the spectral features to determine the proper offset between the individual spectra. The offsets were computed to the nearest corresponding wavelength grid point, and the spectra were directly added together with no noticeable effect on the resolution.

As with all ruled gratings, the GHRS echelles have some degree of imperfection which produces scattered light that can appear as background which must be removed. (For a detailed

---

[1] Washburn Observatory, University of Wisconsin-Madison, 475 North Charter Street, Madison, WI 53706.

[2] Department of Physics, Catholic University of America, Washington, DC 20064

[3] Laboratory for Astronomy and Solar Physics, NASA/Goddard Space Flight Center, Greenbelt, MD 20771.

[4] Ball Aerospace Systems, P.O. Box 1062, Boulder, CO 80306.

1991ApJ...377L..57C

quantitative discussion of the nature of GHRS echelle scattering, see Cardelli et al. 1990a.) The background is measured with the full 500 science diode array on either side of the observed echelle order of interest with an exposure time which is about 10% of the total requested exposure time for the requested observation. Cardelli et al. (1990a) recommend a background correction scheme which combines the measured background and the terms cNi ($Ni \equiv$ per point net spectrum) and dN ($N \equiv$ average of the net spectrum). From the analysis of strongly saturated absorption lines in the ξ Per spectra, we estimate $c \leq 0.01$, and $d \approx 0.03$–0.05 (see Cardelli et al. 1991). We conclude that residual zero-point errors due to scattered light are $\leq 1\%$ of the average net spectrum. This uncertainty is adopted in our analysis.

Possible sources of wavelength assignment errors include (1) uncertainties associated with the wavelengths assigned to a given grating setting and magnetic drift effects produced by Earth's magnetic field (*internal errors*) and (2) uncertainties associated with the compensation for the spacecraft orbital motion (*external errors*). In the absence of wavelength calibration observations, internal errors as large as ± 1 diode (± 4 km s^{-1}) are expected. For the ξ Per data, we found shifts of the order of $\leq \pm 2$ km s^{-1} between observations obtained at different setup wavelengths. To minimize internal wavelength errors, we developed a "bootstrap" correction technique. Basically, alignment of all the features of a given species (e.g., Fe II and Si II) allowed us to determine relative wavelength (velocity) shifts for other species that had transitions present in the same spectrum. Structure in the stronger lines of Si II and Fe II allowed us to reference these two species together. Application of this technique allowed us to derive wavelength corrections for all the species discussed here.

One of the January observations included in our "bootstrap," centered on 1302 Å, included two telluric O I lines which should have a velocity, corresponding to the component of Earth's rotation in the direction the spacecraft was pointed, of -0.4 km s^{-1}. We measured a velocity of -2.8 km s^{-1} for the two telluric lines indicating that a correction of $+2.4$ km s^{-1} must be added to the "bootstrapped" wavelengths. We estimate the uncertainty of our corrected heliocentric wavelength scale to be $\leq \pm \frac{1}{8}$ diode (± 0.5 km s^{-1}).

In the analysis presented here, we restrict our discussion to (1) absorption arising over the heliocentric velocity range of $+5 \leq v_{\odot} \leq +20$ km s^{-1}, and (2) absorption lines with mean optical depths of <3 ($W_\lambda \leq 100$ mÅ). Examples of some of the observed diffuse cloud absorption line profiles are shown in Figure 1 plotted against heliocentric velocity. Of particular note is the detection of the weak intersystem line of C II] λ2325 (see the note at the end of Table 1). Some information on the diffuse cloud absorption lines analyzed here are listed in Table 1. The quoted equivalent width errors listed in Table 1 were derived from the combination of the point-to-point statistical uncertainty in the data, uncertainty associated with continuum placement (see Cardelli et al. 1990b, 1991; Sembach, Savage, & Massa 1991), and uncertainty in the scattered light correction.

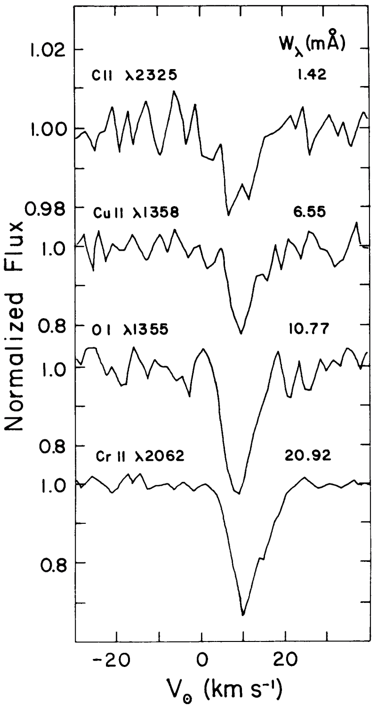

FIG. 1.—Examples of dominant ion absorption-line profiles, plotted against heliocentric velocity, for the sight line to ξ Per. The line species/wavelengths are shown on the left, while the derived equivalent widths (mÅ) are shown on the right. The continuum signal-to-noise ratio for the weak C II] detection is 160/1.

TABLE 1

UNSATURATED OR MILDLY SATURATED LINES FROM THE DOMINANT IONIZATION STAGE

Species	λ_0 (Å)[a]	$\log f\lambda$[b]	W_λ[c] ($\pm 1\ \sigma$)	S/N[d]
C II][e]	2325.40	−3.982	1.42 (0.41)	160
O I]	1355.60	−2.772	10.77 (1.26)	26
Mg II	1239.93	−0.479	29.14 (1.74)	15
	1240.40	−0.780	22.00 (1.81)	16
P II	1301.87	1.351	31.88 (0.82)	35
	1532.53	1.067	22.62 (4.10)	10
Cr II	2062.23	2.340	20.92 (0.83)	82
	2066.16	2.164	13.93 (0.76)	80
Mn II	2305.71	0.456	1.73 (0.60)	71
	2606.46	2.701	116.02 (1.47)	82
Fe II	2249.88	0.752	36.13 (3.44)	17
	2260.71	0.924	42.30 (2.99)	19
Ni II	1370.13	2.254	19.22 (2.00)	26
	1804.47	1.111	2.87 (0.72)	63
Cu II	1358.77	2.211	6.55 (1.00)	28
Zn II	2026.46	3.018	99.74 (1.13)	83
	2062.66	2.717	84.33 (1.28)	75

[a] Rest vacuum wavelength from Morton 1991.

[b] Product of f-value and rest wavelength from Morton 1991.

[c] Measured equivalent width and $\pm 1\ \sigma$ error (in mÅ).

[d] Signal-to-noise derived from the continuum rms.

[e] Only three of the four FP-SPLIT subexposures were used due to the presence of a fixed pattern noise element.

3. THE DIFFUSE CLOUD TOWARD ξ PERSEI

To study the component structure exhibited in this sight line (see Fig. 1), we have chosen to analyze the data by expressing the observed line profiles in the form of apparent optical depth profiles versus velocity (see Jenkins et al. 1989; Joseph & Jenkins 1990; Savage & Sembach 1991; Savage et al. 1991).

The velocity-dependent apparent column density, $N_a(v)$, takes the form

$$N_a(v) = (m_e c/\pi e^2)\tau_a(v)/f\lambda = [\tau_a(v)/f\lambda]3.768 \times 10^{14}\ \mathrm{cm^{-2}\ km^{-1}\ s}\,, \quad (1)$$

where $\tau_a(v)$ is the natural logarithm of fitted continuum/observed flux, and $f\lambda$ is the product of the oscillator strength and the rest wavelength (in units of Å). In the limit where the line profile is completely resolved, equation (1) expresses the *true* column density distribution *independent of the degree of saturation.* However, at 3.5 km $\mathrm{s^{-1}}$ resolution, many of the narrow components present in the data may not be resolved, and so the presence of saturated unresolved structure can potentially distort the apparent column density profiles. The presence of unresolved structure can be explored by comparing two or more line profiles of the same species, whose $f\lambda$ values are reasonably different, in log $N_a(v)$. When saturated unresolved structure is present, the two profiles diverge from each other over the saturated region (see Savage & Sembach 1991). With the exception of the doublets of Mg II (λ1240), Zn II, and possibly Mn II λ2606, comparison of the profile pairs listed in Table 1 indicates no unresolved structure within the errors. Consequently, these profiles can be directly compared or integrated to obtain total column densities.

3.1. *Integrated Cloud Characteristics: Column Densities and Depletions*

One approach to analyzing the data is through expressing the results as integrated column densities. Although we discard important velocity information, presenting column density information in this way is still useful, especially for comparison to the large volume of data in the literature that have been presented in this fashion. The logarithm of the derived total column densities of the species listed in Table 1 are given in Table 2 along with the $\pm 1\ \sigma$ errors. These errors were determined using the same three sources of uncertainties described above in § 2. For Mg II and Zn II doublets, a "column density correction" was applied to the weaker of the integrated profile values using the "doublet correction" procedure described by Savage & Sembach (1991). For Mg II and Zn II, the correction amounted to a factor of 1.36 and 1.12, respectively. For Mn II λ2606, one suspects that saturated unresolved

TABLE 2

INTEGRATED COLUMN DENSITIES OF DOMINANT DIFFUSE CLOUD IONS

SPECIES	STATE[a]	log COLUMN DENSITY[b] Best	$+1\ \sigma$	$-1\ \sigma$	$A_\odot$[c]	METHOD[d]
C	II	17.81	17.92	17.67	−3.44	1, 3
		17.65	17.82	17.38		2
O	I	17.78	17.83	17.72	−3.07	3
		17.93	18.07	17.74		2
Mg	II	16.32	16.36	16.28	−4.41	4
		15.82	15.90	15.73		2
P	II	14.26	14.28	14.23	−6.43	3
Cr	II	12.76	12.77	12.74	−6.32	3
Mn	II	13.51	13.53	13.48	−6.47	1, 3, 5
Fe	II	14.56	14.59	14.53	−4.49	3
Ni	II	13.09	13.13	13.04	−5.75	1, 3
Cu	II	12.54	12.60	12.47	−7.73	3
Zn	II	13.38	13.40	13.37	−7.35	4

[a] Ionization state of observed lines (I ≡ neutral, II ≡ first ion).

[b] Logarithm of derived column density ($\mathrm{cm^{-2}}$) and $\pm 1\ \sigma$ errors (see text).

[c] Logarithm of solar elemental abundances relative to hydrogen (from Morton 1991). For ξ Per, log $N(\mathrm{H_{total}}) \equiv \log\ [N(\mathrm{H\ I}) + 2N(\mathrm{H_2})] = 21.29$ (Bohlin, Savage, & Drake 1978).

[d] Method used to derive column densities and errors: 1 ≡ weak line limit, 2 ≡ damping wings, 3 ≡ direct profile integration, 4 ≡ direct profile integration corrected for "doublet" saturation, 5 ≡ "saturation correction" determined from curve-of-growth fit.

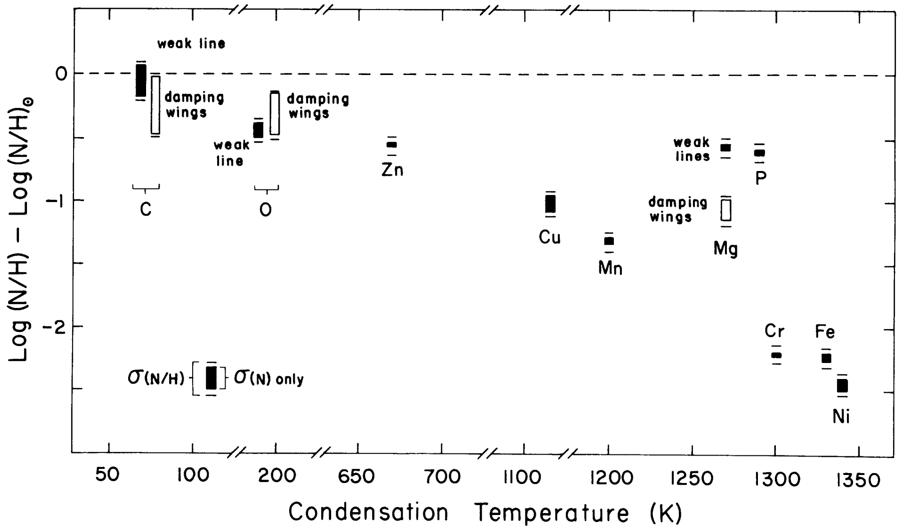

FIG. 2.—Mean depletions for the dominant ions arising in the diffuse clouds toward ξ Per plotted against condensation temperature (Jenkins 1987). The filled symbols correspond to the range of depletions derived from the $\pm 1\ \sigma$ column density (N) limits listed in Table 2 obtained by integrating the $N_a(v)$ profiles. The total hydrogen column density, H, was taken from Bohlin, Savage, & Drake (1978). The open symbols were obtained from the $\pm 1\ \sigma$ column density limits found from an analysis of the damping wings of the strongly saturated lines of C II (λ1334), O I (λ1302), and Mg II ($\lambda\lambda$2796/2803). The horizontal lines correspond to the depletion limits if we include the uncertainty in the total hydrogen column density. The discrepancy between the open and filled symbols, especially for Mg II, indicates the existence of errors in the adopted oscillator strengths (Morton 1991).

structure is present and so we derived a saturation correction by using the results of a curve of growth fit to the two lines. Finally, we also present results derived from strongly saturated lines of C II λ1335, O I λ1302, and the Mg II doublet at λ2796/2803. These lines exhibit damping wings, and so column densities were derived using the continuum reconstruction method (Bohlin 1975) with *f*-values and damping constants taken from Morton (1991).

Also listed in Table 2 are the adopted solar elemental abundances from Morton (1991). From Bohlin et al. (1978) we find $N(\mathrm{H_{total}}) \equiv [N(\mathrm{H\ I}) + 2N(\mathrm{H_2})] = 1.97 \times 10^{21} \pm 3.5 \times 10^{20}\ \mathrm{cm^{-2}}$. From these data, we derive mean diffuse cloud depletions which are shown in Figure 2. Given the accuracy of the derived depletions, one must now carefully consider the relative uncertainties inherent in the adopted solar abundances. For example, while the most commonly accepted solar value for $N(\mathrm{C})/N(\mathrm{H}) = 3.6 \times 10^{-4}$ (Anders & Grevasse 1989), values as high as 4.5×10^{-4} have been suggested (Meyer 1988). Given the importance of carbon depletion to theories of interstellar dust, the appropriate value for the reference abundance is an important consideration, especially if we adopt the results of the weak C II] line. Another serious consideration concerns the quality of oscillator strengths. Consider the case for C, O, and Mg. Although the weak lines appear to more tightly constrain the column densities, the *f*-values for these transitions are more uncertain than for the strong transitions as noted by Morton (1991). The most prominent example is Mg II: the column density derived from weak λ1240 doublet is more than a factor of 3 larger than for the strong λ2800 doublet. Because the ratio of *f*-values between the lines of a doublet are fairly well known, the source of error is in the absolute *f*-values of the pair, most likely λ1240. The high quality of the GHRS data suggests that attention must now focus on determining accurate atomic constants.

3.2. *Velocity-dependent Characteristics*

To examine possible variations in depletion, as well as ionization and density we have chosen to examine $N_a(v)$ profiles for a few species that cover a large range of physical conditions and depletions as implied by the data in Figure 2. We examine a pair of neutral lines (S I λ1807, C I* λ1194) arising from relatively lightly depleted species, a pair of dominant ion lines from lightly depleted species (Zn II λ2062, O I λ1355), and a pair of dominant ion lines from heavily depleted species (Cr II λ2062, Fe II λ2260). These profiles are shown in Figure 3 plotted against heliocentric velocity. The vertical alignment of the profiles was chosen so that the left wings of all the profiles overlapped.

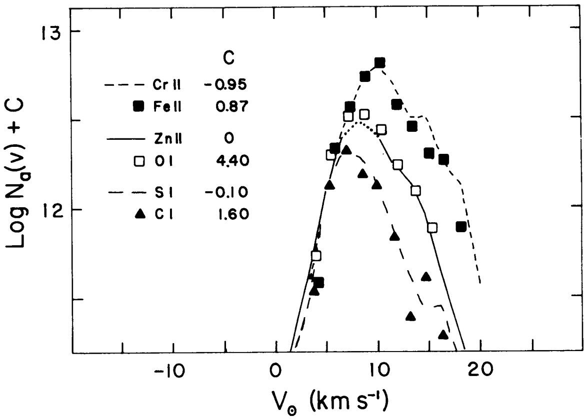

FIG. 3.—Comparison between log $N_a(v)$ profiles for neutral lines from lightly depleted species [S I (*long dash line*), C I (*filled triangles*)], dominant ion lines from lightly depleted species [Zn II (*solid line*), O I (*open squares*)], and dominant ion lines from heavily depleted species [Cr II (*short dashed line*), Fe II (*filled squares*)]. The dotted portion of the Zn II profile corresponds to the presence of possible unresolved saturation. The scaling for the individual profiles can be recovered by adding the constant *C* to the vertical scale. The increasing profile width and shift in peak log $N_a(v)$ can be interpreted as both a decrease in gas density *and* depletion for $v_\odot > 7$ km s^{-1}.

For each of the regimes we have chosen to represent, each pair of profiles agrees very well. However, as one progresses from neutral through dominant ion/lightly depleted on out to dominant ion/heavily depleted species, the profiles become noticeably broader and the velocity where the maximum of $N_a(v)$ occurs systematically shifts toward large positive velocities. *We interpret this as indicating a decrease in both density and depletion.* Specifically, for $v_\odot > 7$ km s^{-1}, Cr and Fe are significantly less depleted relative to Zn and O by as much as a factor 2 or more than for $v_\odot < 7$ km s^{-1}.

We thank the many dedicated people involved in the GHRS project. Data handling support from Marilyn Meade and Brian Babler is highly appreciated. J. A. C. and B. D. S. acknowledge support for their involvement with the GHRS through NASA contract NAS5-29638. D. C. E. acknowledges support through NASA contract NAS5-26000.

REFERENCES

Anders, E., & Grevasse, N. 1989, Geochem. Cosmochem. Acta, 53, 197
Bohlin, R. C. 1975, ApJ, 200, 402
Bohlin, R. C., Savage, B. D., & Drake, J. F. 1978, ApJ, 224, 132
Cardelli, J. A., Ebbets, D. C., & Savage, B. D. 1990a, ApJ, 365, 789
Cardelli, J. A., Savage, B. D., Sofia, U. J., & Sembach, K. R. 1991, in preparation
Cardelli, J. A., Suntzeff, N. B., Edgar, R. J., & Savage, B. D. 1990b, ApJ, 362, 551
Duncan, D. K., & Ebbets, D. C. 1989, Goddard High Resolution Spectrograph Instrument Handbook (Baltimore: Space Telescope Science Institute)
Gomez-Gonzalez, J., & Lequeux, J. 1975, A&A, 38, 29
Hobbs, L. M. 1974, ApJ, 188, L67
Jenkins, E. B. 1987, in Interstellar Processes, ed. D. J. Hollenbach & H. A. Thronson (Dordrecht: Reidel) 533
Jenkins, E. B., Lees, J. F., van Dishoeck, E. F., & Wilcots, E. M. 1989, ApJ, 343, 785
Joseph, C. L., & Jenkins, E. B. 1990, ApJ, 368, 201
Marschall, L. A., & Hobbs, L. M. 1972, ApJ, 173, 43
Meyer, J.-P., 1988, in Origins of the Elements, ed. G. J. Mathews (Singapore: World Scientific), 337
Morton, D. C. 1991, ApJS, in press
Savage, B. D., Cardelli, J. A., Bruhweiler, F. C., Smith, A. M., Ebbets, D. C., & Sembach, K. R. 1991, ApJ, submitted
Savage, B. D., & Sembach, K. R. 1991, ApJS, submitted
Sembach, K. R., Savage, B. D., & Massa, D. 1991, ApJ, 372, 81
Stokes, G. M. 1978, ApJS, 36, 115